The Multi-Segment Complexity of the 2024 M_W 7.5 Noto Peninsula Earthquake Governs Tsunami Generation

Fabian Kutschera[1], Zhe Jia[2,1], Bar Oryan[1], Jeremy Wing Ching Wong[1], Wenyuan Fan[1], Alice-Agnes Gabriel[1,3]

[1]Institute of Geophysics and Planetary Physics, Scripps Institution of Oceanography, University of California San Diego, La Jolla, USA
[2]Institute for Geophysics, Jackson School of Geosciences, The University of Texas at Austin, Austin, USA
[3]Department of Earth and Environmental Sciences, Ludwig-Maximilians-Universität München, Munich, Germany

Key Points:

- The earthquake ruptures bilaterally, including six subevents, and delayed re-nucleation at its hypocenter, consistent with fault weakening.
- Our multi-fault subevent model aligns with known fault system geometries and is critical in explaining the observed tsunami.
- Analysis of alternative source models and 2000 multi-CMT solutions shows complex source effects are important for realistic tsunami models.

Corresponding author: Fabian Kutschera, fkutschera@ucsd.edu

Abstract

The January 1st, 2024, moment magnitude (M_W) 7.5 Noto Peninsula earthquake ruptured in complex ways, challenging analysis of its tsunami generation. We present tsunami models informed by a 6-subevent centroid moment tensor (CMT) model obtained through Bayesian inversion of teleseismic and strong motion data. We identify two distinct bilateral rupture episodes. Initial, onshore rupture towards the southwest is followed by delayed re-nucleation at the hypocenter, likely aided by fault weakening, causing significant seafloor uplift to the northeast. We construct a complex multi-fault uplift model, validated against geodetic observations, that aligns with known fault system geometries and is critical in modeling the observed tsunami. The simulations can explain tsunami wave amplitude, timing, and polarity of the leading wave, which are crucial for tsunami early warning. Upon comparison with alternative source models and analysis of 2000 multi-CMT ensemble solutions, we highlight the importance of incorporating complex source effects for realistic tsunami simulations.

Plain Language Summary

The 2024 moment magnitude 7.5 New Year's Day Noto Peninsula earthquake ruptured a complex, partially offshore fault system and generated a tsunami in the Sea of Japan. We use seismic data to show that the earthquake can be characterized by six distinct subevents, with an initial predominantly onshore rupture propagation towards the southwest and a 20-second delayed second rupture onset towards the northeast, mostly offshore. This second rupture episode is critical for the generation of the tsunami. We use the information we gain from these subevents, such as location and faulting mechanism, to infer the seafloor movement, which informs tsunami simulations. The reconstruction of the earthquake rupture process is not unique. This allows us to explore the influence of source uncertainties on the modeled tsunami, highlighting the importance of complex source effects for tsunami generation. The need for complexity in the generation of the tsunami becomes further evident when we compare the solutions against other, rapidly available models of the earthquake. We find that the preferred model matches tsunami onset times, first-motion polarities, and initial wave amplitudes, crucial aspects for tsunami early warning.

1 Introduction

The January 1st, 2024 M_W 7.5 Noto Peninsula (Noto-Hanto) earthquake ruptured an active submarine fault system (Figure 1; MLIT (2014); Sato et al. (2020)) causing strong ground shaking and a large tsunami within the Sea of Japan. Early analysis points to an unusually complex rupture process, with estimated slip distributions differing considerably (Fujii & Satake, 2024; Ma et al., 2024; Masuda et al., 2024; Mizutani et al., 2024; Okuwaki et al., 2024; Yang et al., 2024).

Rapid finite-fault models based on teleseismic data were available within hours after the event (The Headquarters for Earthquake Research Promotion, 2024; U.S. Geological Survey, 2024). The United States Geological Survey (USGS) released a first version obtained solely from the teleseismic data (hereafter model "USGS-T", Supporting Information S1, Figure S1). Later, the USGS released an updated model using both the teleseismic and Global Navigation Satellite System (GNSS) data (hereafter model "USGS-T+G"). This model differs starkly from the earlier version. Specifically, the updated USGS-T+G model does not have significant offshore slip.

Another finite-fault model is obtained using 53 GNSS stations across the Noto Peninsula, placing the majority of slip onshore or near the northern shoreline of Noto Peninsula (Fujii & Satake, 2024). In contrast to the USGS-T+G model, a finite-fault model from tsunami waveforms recorded around the Sea of Japan places most of the slip offshore (Fujii & Satake, 2024). Additionally, Masuda et al. (2024) investigated landslide contributions to local tsunami generation, but precise reconstruction is challenged by the limited regional bathymetry resolution. Source complexity is important for tsunami generation and propagation (Abrahams et al., 2023; Dettmer et al., 2016; Lotto et al., 2018; Wirp et al., 2021). Thus, vastly different source models will have different implications for understanding the observed tsunami generation and early warning.

Many tsunami early warning centers rely on rapid earthquake magnitude estimations using W phase inversions (Kanamori, 1993; Kanamori & Rivera, 2008), which are typically available within minutes to tens of minutes after an earthquake's origin time (Hirshorn et al., 2020; D. Wang et al., 2012). Emerging methods for tsunami warning include seismogeodetic approaches (Golriz et al., 2023), probabilistic tsunami forecasting (Mori et al., 2022; Selva et al., 2021), or more elaborate source descriptions (Melgar et al., 2016), such as moment tensors (Gusman & Tanioka, 2014; Miyoshi et al., 2015) and automated finite fault inversions (Zheng et al., 2020).

This study aims to address the challenge of resolving earthquake rupture complexities and properly translating those complexities to inform accurate tsunami simulations. We present tsunami simulations informed by constructing complex seafloor displacements from a 6-subevent centroid moment tensor (CMT) model based on a Bayesian inversion. We obtain our CMT model using teleseismic and strong motion observations of the Noto Peninsula earthquake and unify seismic and tsunami observations in agreement with geodetic data. To the best of our knowledge, this study is the first to use a multi-CMT model to source a tsunami simulation. We demonstrate that our approach captures key characteristics of the tsunami complexities better than other rapid finite-fault inversion approaches and discuss the effects of source complexity and its uncertainties on tsunami modeling based on an ensemble of 2000 multi-CMT solutions.

2 Methods

2.1 Seismic Multi-Centroid Moment Tensor Inversion

We constrain the event's rupture propagation using a multiple CMT subevent inversion method (Tsai et al., 2005; Minson & Dreger, 2008; Jia et al., 2022, 2023). The inversion process iteratively increases the number of subevents to achieve a 65% waveform misfit reduction (Figures S2-S7). The preferred model includes six subevents, E1 to E6, ordered by their centroid time (Figure 1). Each subevent is characterized by 10 unknowns: centroid time, duration, longitude, latitude, depth, and the five independent components of the symmetric and zero-traced moment tensor (Figures S8, S9, Table S1).

We use a Markov Chain Monte Carlo (MCMC) method with a Metropolis–Hasting accept-reject criterion (Hastings, 1970) to sample the posterior probability density function in a Bayesian framework (Bodin et al., 2012; Sambridge & Mosegaard, 2002; Jia et al., 2023). This MCMC inversion first searches the centroid time, duration, longitude, latitude, and depth and then linearly solves for the independent moment tensor components. We choose bounded uniform prior distributions of all non-linear unknowns except the horizontal locations, for which we set priors based on the first three days of aftershocks (Supporting Information S1, Figure S10). In total, we obtain an ensemble of 240,000 permissible multi-CMT solutions, requiring 920 core hours, a modest demand by modern computing standards. Our iterative approach, which does not require manual calibration, could potentially be deployed in early warning centers when utilizing medium-scale parallel computing in an "urgent supercomputing" setting (e.g., de la Puente et al., 2020) or in combination with machine-learning approaches (e.g., Liu et al., 2021; Rim et al., 2022).

We choose the preferred multi-CMT model based on minimizing the seismic waveform misfit. We use P and SH waveforms from 93 teleseismic stations (Figure S11) within

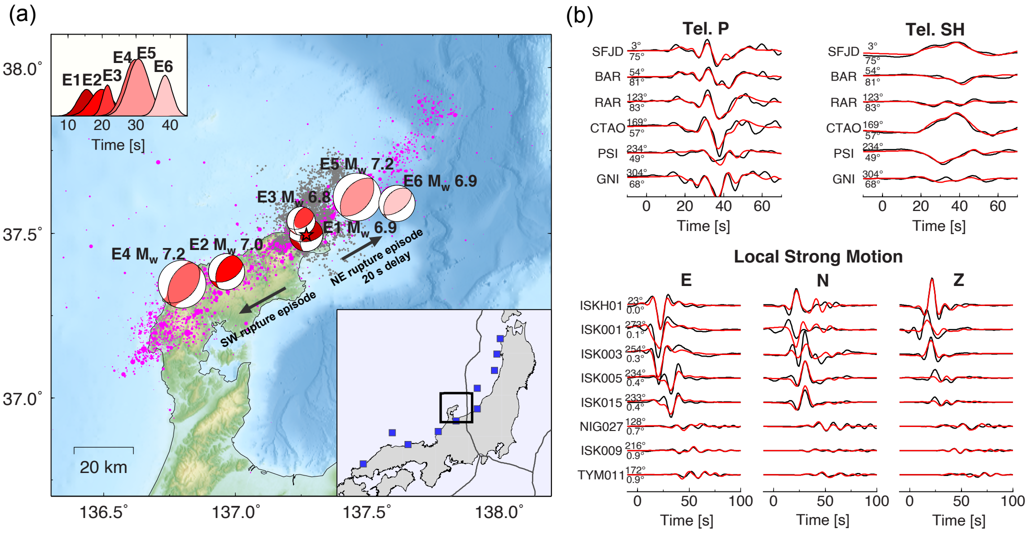

Figure 1. (a) Overview of the Noto Peninsula, Japan, study area. The red star indicates the JMA epicenter of the January 1, 2024, M_W 7.5 Noto Peninsula earthquake. The red focal mechanisms are the six subevents of the Bayesian multi-centroid moment tensor (CMT) inversion using teleseismic and regional strong motion data. The earthquake first initiates towards the southwest, indicated by subevents E1, E2, and E4. After a delay of 20 s, the rupture unfolds towards the northeast, as indicated by subevents E3, E5, and E6. The focal mechanisms are color-coded with respect to time, and the corresponding Gaussian source time durations are shown in the top left figure inset. Pink circles indicate aftershocks up to January 2, 2024 (Japan Meteorological Agency, 2024), and gray circles show mainshock preceding relocated seismicity (Yoshida et al., 2023). The blue squares in the bottom right figure inset mark the position of tide gauges facing the Sea of Japan. (b) Comparison of selected observed (black) teleseismic P, SH (both in displacement), and local strong ground motion recordings (in velocity) with the corresponding synthetic seismic waveforms (red) of the preferred multi-CMT solution. The numbers leading the traces are the respective azimuth and distance.

an epicentral distance range of 30° to 90°, obtained from the EarthScope Data Management Center (DMC; Albuquerque Seismological Laboratory/USGS, 2014). Additionally, we use three-component regional strong ground motion waveforms from KIK-net and K-net stations within an epicentral distance of 150 km, provided by the National Research Institute for Earth Science and Disaster Prevention (NIED; Okada et al., 2004). During the inversion of regional strong motion data, we adopt the JMA2001 1D velocity model (Ueno, 2002), and use a frequency-wavenumber method (L. Zhu & Rivera, 2002) to calculate the Green's functions. For the inversion of teleseismic waves, we calculate the Green's functions with a hybrid method that combines propagator matrix and ray theory (Kikuchi & Kanamori, 1982; Qian et al., 2017), and use a combination of the JMA2001 model for the crust with an IASPEI91 model (Kennett & Engdahl, 1991) describing the deeper earth.

2.2 Mapping the Subevent Model to Seafloor Deformation

We construct a six-fault-segment slip model based on the preferred subevent model (Table S2), assuming rectangular faults. Each fault segment is located at the respective subevent centroid location. We determine their dip, strike, and rake angles from the preferred multi-CMT solution. Following previously reported fault dip directions (Fujii & Satake, 2024; MLIT, 2014), we consider E1-E5 southeast dipping, and E6, located in the northeast of Noto Peninsula, with dip towards the northwest. Each fault segment has an along-strike length of 25 km and extends from the surface with an along-dip depth twice its centroid depth.

Informed by the preferred multi-CMT model, we assume a uniform slip distribution across each of the six fault segments, which we obtain from each respective subevent's seismic moment and an assumed rigidity of 35 GPa, which resembles the mean rigidity of the shallowest 25 km as given by the JMA2001 velocity model (Ueno, 2002) and is similar to the assumed value in Fujii and Satake (2024) and Masuda et al. (2024). We then use an analytic elastic dislocation model (Okada, 1985, 1992) to obtain the corresponding surface displacements and apply the same approach to infer the surface deformation from the two USGS finite-fault models (Supporting Information S1).

To evaluate the uncertainties in surface deformation and its impact on tsunami generation, we repeat this analysis for 2000 randomly selected realizations out of the 240,000 MCMC ensemble solutions (Table S3). We use the sum of the absolute offshore vertical displacement due to the 2000 multi-CMT solutions as a metric to identify two end-member multi-CMT solutions, the minimum and maximum uplift CMT solutions, which yield the least and the most amount of offshore vertical displacements (Figure S12), respectively.

2.3 Tsunami Simulations

We use GeoClaw and the vertical offshore surface deformation as instantaneous sources for tsunami simulations. GeoClaw is part of the open-source software package ClawPack (LeVeque et al., 2011; Berger et al., 2011; Mandli et al., 2016), which solves the 2D depth-averaged non-linear shallow water equations and has been validated against community benchmark problems and real observations (LeVeque & George, 2008; González et al., 2011; Arcos & LeVeque, 2015). The algorithm has been successfully applied to model the 2004 Sumatra tsunami (Ulrich et al., 2022) and the 2017 Tehuantepec tsunami in Mexico (Melgar & Ruiz-Angulo, 2018).

We use gridded bathymetry data (GEBCO Compilation Group, 2023) with a resolution of 15 arc seconds (450 m) and define the sea surface height anomaly (ssha) as the deviation from the ocean surface at rest (Supporting Information S1). We simulate all tsunami scenarios for three hours, with each simulation requiring $\sim$7.5 h on a laptop (MacBook Air with Apple M2 processor). However, GeoClaw can also be run in parallel using shared memory via OpenMP (Mandli et al., 2016) or can be accelerated using GPUs (Qin et al., 2019), potentially enabling better alignment with tsunami early warning requirements.

We validate our simulated tsunami waveforms with sea level observations obtained from the IOC and the GSI, which provide their data with sampling rates of 60 s and 30 s, respectively. First, we use the LOWESS algorithm (Locally Weighted Scatterplot Smoothing; Cleveland, 1979; Romano et al., 2021) to remove first-order tidal trends. Next, we trim the data to three hours after the mainshock origin time (2024-01-01 7:10:22.5 UTC; provided by the JMA) before applying a 300 s lowpass filter. To quantify the similarity of the simulated and observed first-arriving wave packet at the tide gauges, we calculate the cross-correlation coefficient for a 20 min time window, starting 5 min before the respective arrival of the peak of the initial tsunami crest (Table S4).

3 Results

3.1 Multi-event, Multi-segment Rupture of the 2024 M_W 7.5 Noto Earthquake

Our subevent model reveals two distinct rupture episodes (Figure 1). Initially, rupture propagates towards the southwest (subevents E1, E2, and E4), lasting for about 30 s. Following a delay of 20 s, while the southwest rupture is ongoing, the rupture re-nucleates around the hypocenter (E3) and propagates bilaterally towards the northeast direction (E5 and E6) for 15 s. Only the aftershock density distribution is used as prior for the horizontal location of each CMT subevent. Nevertheless, the inferred geometry of our preferred six-fault-segment slip model aligns with regional mapped fault traces (Figure S12; Fujii & Satake, 2024; MLIT, 2014) and spatially coincides with the 32-hour aftershock sequence (Movie S1). The hypocentral subevents E1 and E3 are collocated with four year swarm activity preceding the Noto earthquake (Hubbard & Bradley, 2024; Nishimura et al., 2023; Yoshida et al., 2023).

These six subevents share similar reverse-faulting focal mechanisms, albeit varying significantly in size and duration. The nucleation and re-nucleation subevents, E1 and E3, have the smallest moment magnitudes (both M_W 6.9). The two largest subevents, E4 and E5, each with M_W 7.2, are located near the two endpoints of rupture. The two offshore subevents E5 and E6 in the northeast, particularly the large subevent E5, are essential for accurately fitting the timing and amplitude of the secondary pulses in the P waves (Figures S2, S13, S17). Excluding these two subevents leads to noticeable differences in the regional waveform fits, predominantly at eastward stations within azimuths 0-120 degrees (Figures S7, S14-S16, and S18-20). The total normalized regional strong motion data misfit reduction is ∼25% when accounting for subevent E5 and ∼30% when accounting for both subevents E5 and E6. Subevents E2, E4, and E5 each have a source duration of ∼13 s, while the duration for the other three subevents is shorter and ranges between ∼6-11 s.

Robust estimates of event depth and fault geometry are critical for simulating the surface deformation and associated tsunami. Using the ensemble of 240,000 multi-CMT solutions, we analyze source parameter uncertainties. We find that the subevent depths are well-constrained ($\leq$10 km) for all subevents, with an average standard deviation of 1.17 km. All subevent focal mechanisms, except that of E3, also exhibit low uncertainties in strike, dip and rake, with average standard deviations of 15.9°, 4.9°, and 21.3°, respectively. The geometry of the renucleation subevent E3 has distinctly larger uncertainties, with 88.9°, 14.7°, and 101.1°, in strike, dip, and rake, which likely arise from its concurrence with ongoing southwest rupture, challenging resolution. However, subevent E3 is necessary to explain the closest strong motion waves (Figure S21).

3.2 Complex Onshore and Offshore Surface Deformation

Subevents E1–E4 result in a combination of onshore and offshore surface deformation, while the uplift generated by subevents E5 and E6 is located entirely offshore (Figure 2). The respective northeast rupture episode releases 40% of the seismic moment, translating into up to 5.27 m of offshore fault slip.

The modeled surface displacements resulting from the complex rupture of the Noto earthquake show a peak vertical offshore uplift of 3.76 m. The horizontal and vertical synthetics agree mostly well with the regional GNSS observations (Figure 2a, b), indicating broad uplift across the northern Noto Peninsula, subtle subsidence in the far-field, and predominantly westward horizontal motion of the Noto Peninsula. The root mean square errors between observations and synthetic GNSS displacements in East-West, North-South, and Up-Down components are 0.30 m, 0.20 m, and 0.32 m, respectively.

Vertical GNSS data are often challenging to match accurately with geodetic models, particularly in the context of coseismic deformation, often falling within the noise level, which leads to their frequent omission (e.g., Genrich & Bock, 2006; Tanaka et al., 2019; Tong et al., 2010). The model predicts less vertical motion than the one recorded at station J576. However, both the USGS-T+G model and the finite-fault model from Fujii and Satake (2024) cannot fully capture the amount of observed subsidence at this site either, suggesting it may be affected by local processes such as landslides or liquefaction (Gomez, 2024; Kataoka et al., 2024; Mulia et al., 2024; Suppasri et al., 2024). Our model overestimates vertical displacements at station J053 and underestimates it at station J253, each by a factor of two. At station J971, the model accurately reproduces the observed uplift of ∼1 m, performing better than the USGS-T finite-fault model and is comparable to the USGS-T+G model (Figure 2c, d).

Our predicted subevent surface displacement produces substantial vertical motion offshore compared to the limited amount of uplift suggested by USGS-T+G and USGS-T models (Figure 2). The latter predicts an offshore vertical uplift up to 1.45 m (Figure 2c), while the USGS-T+G model (Figure 2d) predicts a negligible amount of uplift in the northeast of Noto Peninsula. These differences directly affect the tsunami simulations (Section 3.3).

We evaluate the effects of source parameter uncertainties on predicted surface displacement and the associated tsunami simulations. We examine the surface deformations caused by 2000 permissible multi-CMT solutions. The peak offshore uplift varies considerably and has a standard deviation of 1.43 m (Figure 4a). The minimum uplift CMT model locates the subevents E1-E4 further landwards and produces a significantly reduced offshore uplift of up to 3.06 m (Figure S12b). The maximum uplift model locates subevents E1-E4 mostly offshore, leading to a large offshore uplift of up to 4.61 m (Figure S12c).

3.3 Complex Tsunami in the Sea of Japan

Our tsunami simulation shows complex coastal wave behavior (Movie S2), including wave crests bending parallel to the coastline due to refraction at the shoaling bathymetry (Figure 3a). Our simulated tsunami waves capture the timing, initial polarity, and amplitude of the first-arriving crest at all nine tide gauges shown in Figure 3, and the overall shape of the observed tsunami waveforms at most of them. Specifically, the timing, crucial for tsunami early warning, is captured with high accuracy within 1 to 3.5 minutes depending on station distance (Figure 3b), which is comparable to the results of Fujii and Satake (2024) (Figure S22) and superior to the tsunami models using either USGS model (Figure S25). We achieve overall high cross-correlation coefficients (Section 2.3) between the synthetics and observations during the first tsunami wave packet (Figure 3b). However, it is challenging to fully capture the waveform complexity at the tide gauge Toyama (Figure S23).

During the three hours of tsunami propagation modeled, our simulated amplitudes agreed with observations within eight centimeters at Kashiwazaki, Mikuni, Tajiri, Oga, Saigo, and Okushiri stations. At Sado, Tobishima, and Fukaura stations, the fit of early waves is equally good but the model underestimates the amplitudes of later, trailing signals (Figure 4b). The maximum tsunami wave amplitude distribution from our preferred simulation (Figure 4c) indicates large tsunami amplitudes of up to 2.62 m in the source region. Our simulation reveals long-lasting tsunami reverberations around the Noto Peninsula, appearing after 1 hour and 12 minutes (Figure 3a, Movie S2). Such reverberations may be caused by trapped waves, causing energetic edge waves and/or shelf resonance, as has been observed during the tsunami caused by the M_W 8.2 Tehuantepec, Mexico, earthquake (Melgar & Ruiz-Angulo, 2018).

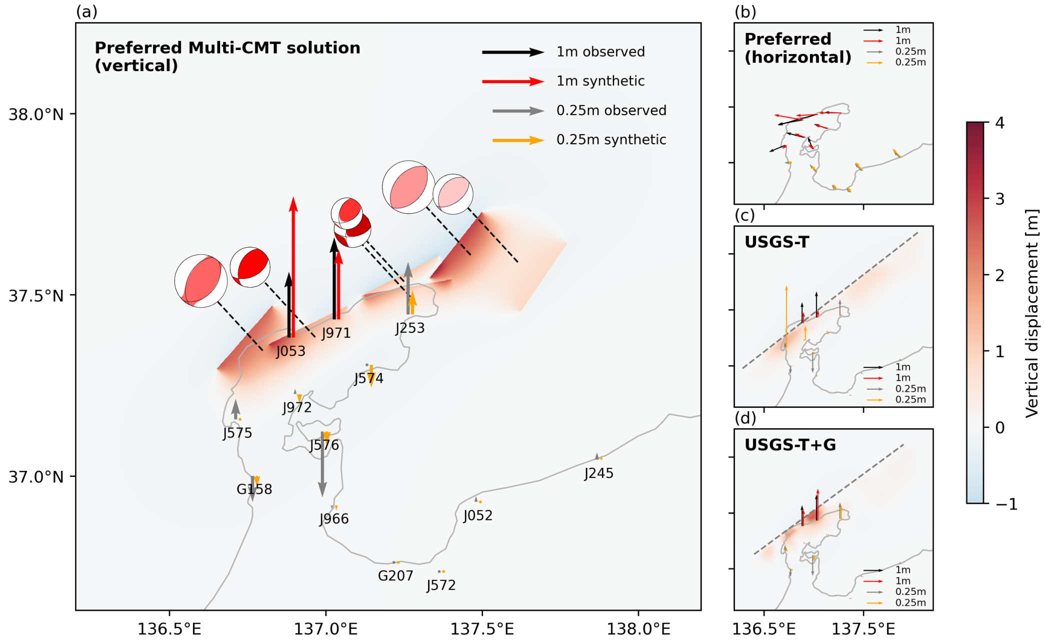

Figure 2. Synthetic vertical displacement constructed from the preferred multi-CMT model using an Okada approach, with a comparison of observed versus synthetic displacements at GNSS sites: (a) vertical and (b) horizontal. Also shown are the vertical displacements from (c) the USGS-T and (d) the USGS-T+G finite-fault models. The six subevents of the preferred multi-CMT solution are indicated by their moment-tensor solutions. Gray lines in panels (c), (d) represent the fault trace of the respective USGS finite-fault model.

The tsunami simulation sourced by the minimum-uplift endmember of our source model ensemble underestimates tsunami amplitudes (peak 2.54 m; Figure 4d, Figure S24, Table S5). In distinction, the tsunami corresponding to the maximum uplift source yields a 46% larger peak tsunami amplitude of up to 3.84 m compared to our preferred tsunami model (Figure 4e). Both rapidly available USGS source models generate localized tsunami (Figure 4b, f, g), but neither can explain the observed tsunami amplitudes and timing (Figure S25).

4 Discussion

An active seismic swarm preceded the M_W 7.5 Noto earthquake (Nishimura et al., 2023), recorded by a dense regional seismic network including events down to magnitude -3 (Hubbard & Bradley, 2024; Japan Meteorological Agency, 2024). Dominated by earthquakes at depths of 14-16 km this swarm led to over 70 mm of surface uplift (Nishimura et al., 2023). Since November 2020, the swarm's activity has fluctuated, including a period of quiescence followed by a M_W 6.2 earthquake in May 2023, the largest event prior to the 2024 Noto earthquake (Kato, 2024; Kato & Nishimura, 2024). During the two weeks leading up to the main shock, a foreshock sequence developed, localizing within a 1 km radius of what would form the Noto earthquake's hypocenter within one hour before its origin time (Kato & Nishimura, 2024).

The spatial and temporal correlation between the swarm activity and the Noto earthquake suggests that the upwelling fluids may have contributed to the event's rupture complexity (Shelly, 2024; Yoshida et al., 2023). Multiple finite-fault models have been pro-

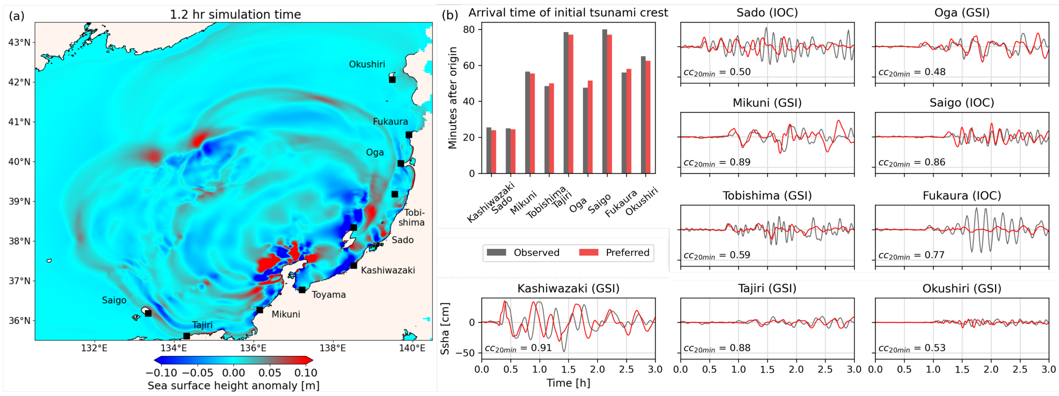

Figure 3. (a) Snapshot of tsunami propagation 1 hour and 12 minutes after the earthquake origin time, showing strong tsunami reverberations surrounding the Noto Peninsula. At this time, the tsunami has reached the tide gauges at Oga and Tobishima to the northeast and the tsunami front is arriving at the Saigo and Tajiri tide gauges to the southwest. (b) Comparison of observed and simulated tsunami arrival times, along with a comparison of tsunami waveforms at nine tide gauges. The stations are ordered by their geodetic distance from subevent E1 (Figure 1).

posed for the Noto earthquake, with differences likely arising from variations in inversion techniques, such as whether multiple slip episodes are permitted, and the relative emphasis on fitting geodetic versus seismic data (Fujii & Satake, 2024; Ma et al., 2024; Okuwaki et al., 2024; Xu et al., 2024; Yang et al., 2024). Ma et al. (2024) propose a slow initial rupture speed of 0.5 km/s for the first 15–20 s, which appears necessary to explain the near-fault strong motion observations. Alternatively, Xu et al. (2024) and records from the closest local strong ground motion stations (e.g., ISKH01 and ISK001, Figure S21) suggest that the hypocentral region experiences a re-rupturing slip episode during the same earthquake. Specifically, the smallest, re-rupturing subevent E3 resolved in our model, which has a centroid time of 21 s after the origin time and releases 7% of the total seismic moment, aligns with the finite-fault model proposed by Okuwaki et al. (2024). Renucleation of slip has been observed in laboratory experiments (Nielsen et al., 2010) and during other large earthquakes (Lee et al., 2006; Wald et al., 1990), including the 2011 Tohoku-Oki event (Lee et al., 2011; Yao et al., 2011; Yagi & Fukahata, 2011). Moreover, theoretical and numerical analysis suggests that weakened faults can offer a physics-based explanation of this effect (Gabriel et al., 2012; Nielsen & Madariaga, 2003).

Earthquake swarms have been linked to aseismic slip or fluid migration (Lohman & McGuire, 2007; Ross et al., 2020). Related cyclic changes in pressure, permeability and fluid migration have been observed in a wide range of fault settings (e.g., Gosselin et al., 2020; Ross et al., 2020; Zal et al., 2020). Here, upward fluid migration due to fault valving (Kato, 2024; Sibson, 1992; W. Zhu et al., 2020) may have aided not only the nucleation but also the rupture and tsunami complexity of the 2024 Noto events. The permeability of the Noto fault system could have been low during its late interseismic period, allowing high pore-fluid pressure to effectively weaken the fault (Madden et al., 2022; Rice, 1992).

Well recorded moderate and large earthquakes have been shown to rupture complex fault networks in a variety of tectonic settings, involving subevents with distinct fault geometries (Hamling et al., 2017; Jia et al., 2023; Taufiqurrahman et al., 2023; Xu et al., 2023). We find that the Noto earthquake included six subevents rupturing multiple fault segments with different configurations: while the first five subevents likely break faults dipping towards the southeast direction, subevent E6 occurs on a northwest-dipping fault.

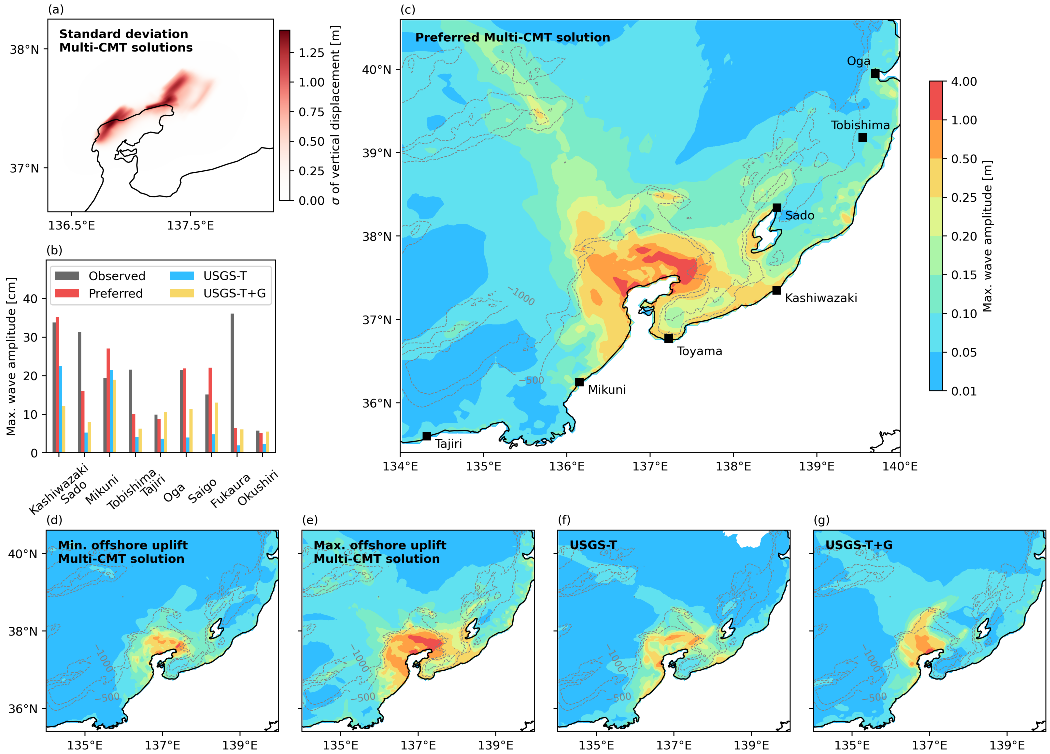

Figure 4. (a) Standard deviation of the vertical displacements based on an ensemble of 2000 multi-CMT solutions. (b) Histogram of the observed and simulated maximum wave amplitudes over a three-hour time window after the earthquake's origin time at the tide gauge locations shown in Figure 3a. (c) Tsunami maximum wave amplitude distribution, sourced by the preferred multi-CMT solution. (d), (e) Tsunami maximum wave amplitude distributions based on the minimum and maximum uplift multi-CMT solutions, respectively. (f), (g) Tsunami maximum wave amplitude distributions modeled using the USGS-T and USGS-T+G source models, respectively.

This dip-change aligns with a two-segment finite-fault model by Okuwaki et al. (2024), which incorporates information on fault orientation. Such complexity may reflect the region's intricate tectonic setting, characterized by the transition between right-lateral strike-slip faults and thrust faults in proximity to the Toyama Trough (Ishiyama et al., 2017; Oike & Huzita, 1988). Excluding subevent E5 from the model results in failure to reproduce the tsunami waveforms, with the most pronounced discrepancy at Kashiwazaki, where the maximum amplitude is underestimated by 47% (Figure S26). Thus, a substantial moment release towards the northeast, i.e., offshore, may be necessary not only for a better fit to seismic waveforms but also for accurate tsunami generation (Figures S26, S27). This significant offshore slip in the North may not be well captured by the onshore GNSS network. However, a recent bathymetric survey by Okamura et al. (2024) reports uplift ranging between 1–4 m along the northern coast of Noto Peninsula, overall consistent with the preferred dislocation model (Figure S28).

To construct the preferred dislocation model, we assume along-strike fault lengths of 25 km with an along-dip depth from the surface to twice its centroid depth for each multi-CMT subevent, respectively. Tsunami early warning centers typically use empirical scaling relations to infer fault dimensions (Hirshorn et al., 2020). While scaling relations for multi-fault earthquakes are elusive, we adapt the fault dimension scaling relation of Leonard (2010) to construct an alternative source model with variable along-strike fault lengths, where we relax the assumption of surface rupture (Supporting Information S1; Figures S29, S30). Five out of the six subevents (E1-E5) yield surface-breaching slip, consistent with the preferred model. The peak vertical displacement is reduced by approximately 40% because the surface deformation is distributed across a broader area of the seafloor due to the longer along-strike length of the faults. Despite these differences, the synthetic tsunami waveforms remain comparable (Figure S31), indicating that the competing effects of broader seafloor deformation and reduced peak uplift counterbalance each other. To better understand the expected variability in uncertain fault dimensions (Satake et al., 2022), and specifically between surface and buried fault slip, we calculate the fault dimensions of all 2000 multi-CMT solutions based on the adapted scaling relation approach. The subfaults associated with subevents E1-E5 cause predominantly ($\geq$70%) surface rupture, while the fault widths calculated from subevent E6 reach the surface in 57% of the cases.

Multi-CMT source inversions have been applied to image tsunamigenic events in different tectonic regimes, such as large megathrust interface earthquakes (e.g., Tsai et al., 2005). To adopt our approach to different tectonic regimes, different scaling relations can be considered (e.g., for subduction interface earthquakes, Allen and Hayes (2017); Murotani et al. (2013)).

Our subevent model demonstrates that resolving the moment release and associated fault location and first-order geometry is critical to inform tsunami rapid response efforts. Our tsunami simulation can explain the initial tsunami wave packets at most stations. However, local discrepancies remain, including underestimating the observed tsunami heights at stations Fukaura and Toyama Bay, which are likely due to (i) limited resolution of bathymetry; and/or (ii) unmodeled effects of landslides. Bathymetry uncertainties are expected to have less impact on leading waves and their arrival times than on the trailing waves (Sepúlveda et al., 2020). Extensive landsliding has been reported shortly after the Noto Peninsula earthquake (Gomez, 2024; Matsushi, 2024; Suppasri et al., 2024), which may have locally affected the tsunami within Toyama Bay (Fujii & Satake, 2024; Koshimura et al., 2024; Masuda et al., 2024; Mulia et al., 2024).

5 Conclusions

In this study, we unravel the complex rupture dynamics of the 2024 M_W 7.5 Noto Peninsula earthquake using a 6-subevent centroid moment tensor model that we obtain from teleseismic and strong motion Bayesian inversion. We observe two distinct rupture episodes: an initial, onshore rupture towards the southwest followed by a subsequent, partly offshore rupture towards the northeast, which re-nucleates at the earthquake's hypocenter after a 20-second delay and causes significant seafloor uplift releasing 40% of the total seismic moment. Using the complex subevent model to simulate the resultant coastal tsunami yields large tsunami wave amplitudes of up to 2.62 m in the source region. Our simulation accurately captures tsunami first arrival timing and overall wave amplitudes. Upon comparison with alternative source models, our findings imply the necessity of using accurate earthquake models that incorporate realistic fault geometries for rapid tsunami modeling and early warning.

Open Research

The 2000 multi-CMT solutions subsampled from the ensemble of 240,000 permissible multi-CMT solutions and all data required to reproduce the tsunami simulations can be found in an openly available Zenodo repository (Kutschera et al., 2024).

The original tide gauge data are obtained from the Intergovernmental Oceanographic Commission (IOC; `http://www.ioc-sealevelmonitoring.org`; last access: 22 August 2024) and from the Geospatial Information Authority of Japan (GSI; `https://www.gsi.go.jp/kanshi/tide_furnish.html`; last access: 22 August 2024). GeoClaw has been used for tsunami modeling (Clawpack Development Team, 2023). Our teleseismic data are from EarthScope (formerly IRIS) DMC (Albuquerque Seismological Laboratory/USGS, 2014). Regional strong motion data comes from the NIED strong-motion seismograph networks K-net and KIK-net (Okada et al., 2004). Statsmodels (Seabold & Perktold, 2010) and ObsPy (Beyreuther et al., 2010; Krischer et al., 2015) were used for data processsing, Matplotlib (Hunter, 2007) and the Generic Mapping Tools (Wessel, 2024) for plotting. The geodetic data are obtained from Nevada Geodetic Laboratory (`http://geodesy.unr.edu`, last access: 22 August 2024) and GEONET, which is operated by the GSI.

Acknowledgments

We thank Ryo Okuwaki, Ignacio Sepúlveda, Jorge Macías Sánchez, and Thomas Ulrich for fruitful discussions. We thank the Editor Germán Prieto, Associate Editor, and two anonymous reviewers for their evaluation and constructive comments. We thank the IOC and the GSI for making the sea level recordings at the tide gauges in the Sea of Japan freely available as well as Yushiro Fujii and Kenji Satake for their tsunami synthetics. The authors acknowledge funding from the National Science Foundation (grant nos. EAR-2225286, EAR-2121568, OAC-2139536, OAC-2311208, EAR-2022441, EAR-2143413), from the European Union's Horizon 2020 research and innovation programme (TEAR ERC Starting; grant no. 852992) and Horizon Europe (ChEESE-2P, grant no. 101093038; DT-GEO, grant no. 101058129; and Geo-INQUIRE, grant no. 101058518), the National Aeronautics and Space Administration (grant no. 80NSSC20K0495) and the Green's Foundation at IGPP at SIO. We acknowledge the Gauss Centre for Supercomputing e.V. (`www.gauss-centre.eu`, project pn49ha) for funding this project by providing computing time on the GCS Supercomputer SuperMUC-NG at Leibniz Supercomputing Centre (`www.lrz.de`).

References

Abrahams, L. S., Krenz, L., Dunham, E. M., Gabriel, A.-A., & Saito, T. (2023). Comparison of methods for coupled earthquake and tsunami modelling. *Geophysical Journal International*, *234*(1), 404–426. doi: 10.1093/gji/ggad053

Albuquerque Seismological Laboratory/USGS. (2014). *Global seismograph network (GSN - IRIS/USGS)* [dataset]. International Federation of Digital Seismograph Networks. doi: 10.7914/SN/IU

Allen, T. I., & Hayes, G. P. (2017). Alternative Rupture-Scaling Relationships for Subduction Interface and Other Offshore Environments. *Bulletin of the Seismological Society of America*, *107*(3), 1240–1253. doi: 10.1785/0120160255

Arcos, M. E., & LeVeque, R. J. (2015). Validating Velocities in the GeoClaw Tsunami Model Using Observations near Hawaii from the 2011 Tohoku Tsunami. *Pure and Applied Geophysics*, *172*(3-4), 849–867. doi: 10.1007/s00024-014-0980-y

Bayes, T. (1763). An essay towards solving a problem in the doctrine of chances. *Philosophical transactions.*, *53*, 370–418.

Berger, M. J., George, D. L., LeVeque, R. J., & Mandli, K. T. (2011). The GeoClaw software for depth-averaged flows with adaptive refinement. *Advances in Water Resources*, *34*(9), 1195–1206. doi: 10.1016/j.advwatres.2011.02.016

Beyreuther, M., Barsch, R., Krischer, L., Megies, T., Behr, Y., & Wassermann, J. (2010). ObsPy: A Python Toolbox for Seismology. *Seismological Research Letters*, *81*(3), 530–533. doi: 10.1785/gssrl.81.3.530

Bodin, T., Sambridge, M., Gallagher, K., & Rawlinson, N. (2012). Transdimensional inversion of receiver functions and surface wave dispersion. *Journal of Geophysical Research: Solid Earth*, *117*(B2). doi: 10.1029/2011JB008560

Clawpack Development Team. (2023). *Clawpack v5.9.2* [software]. Zenodo. doi: 10.5281/zenodo.10076317

Cleveland, W. S. (1979). Robust Locally Weighted Regression and Smoothing Scatterplots. *Journal of the American Statistical Association*, *74*(368), 829–836.

de la Puente, J., Rodriguez, J. E., Monterrubio-Velasco, M., Rojas, O., & Folch, A. (2020). Urgent Supercomputing of Earthquakes: Use Case for Civil Protection. In *Proceedings of the Platform for Advanced Scientific Computing Conference* (pp. 1–8). New York, NY, USA: Association for Computing Machinery. doi: 10.1145/3394277.3401853

Dettmer, J., Hawkins, R., Cummins, P. R., Hossen, J., Sambridge, M., Hino, R., & Inazu, D. (2016). Tsunami source uncertainty estimation: The 2011 Japan tsunami. *Journal of Geophysical Research: Solid Earth*, *121*(6), 4483–4505. doi: 10.1002/2015JB012764

Dreger, D., & Woods, B. (2002). Regional distance seismic moment tensors of nuclear explosions. *Tectonophysics*, *356*(1), 139–156. doi: 10.1016/S0040-1951(02)00381-5

Ekström, G., Nettles, M., & Dziewoński, A. M. (2012). The global CMT project 2004–2010: Centroid-moment tensors for 13,017 earthquakes. *Physics of the Earth and Planetary Interiors*, *200-201*, 1–9. doi: 10.1016/j.pepi.2012.04.002

Flanders Marine Institute (VLIZ), Intergovernmental Oceanographic Commission (IOC). (2024). *Sea level station monitoring facility.* Retrieved from `https://www.ioc-sealevelmonitoring.org` doi: 10.14284/482

Fujii, Y., & Satake, K. (2024). Slip distribution of the 2024 Noto Peninsula earthquake (MJMA 7.6) estimated from tsunami waveforms and GNSS data. *Earth, Planets and Space*, *76*(1), 44. doi: 10.1186/s40623-024-01991-z

Gabriel, A.-A., Ampuero, J.-P., Dalguer, L. A., & Mai, P. M. (2012). The transition of dynamic rupture styles in elastic media under velocity-weakening friction. *Journal of Geophysical Research: Solid Earth*, *117*(B9). doi: 10.1029/2012JB009468

GEBCO Compilation Group. (2023). *GEBCO 2023 Grid* [dataset]. doi: 10.5285/f98b053b-0cbc-6c23-e053-6c86abc0af7b

Genrich, J. F., & Bock, Y. (2006). Instantaneous geodetic positioning with 10–50 Hz GPS measurements: Noise characteristics and implications for monitoring networks. *Journal of Geophysical Research: Solid Earth*, *111*(B3). doi: 10.1029/2005JB003617

Geospatial Information Authority of Japan (GSI). (2024). *Tide level data provided by Geospatial Information Authority of Japan List of tidal stations (in Japanese).* Retrieved from `https://www.gsi.go.jp/kanshi/tide_furnish.html`

Goldberg, D. E., Koch, P., Melgar, D., Riquelme, S., & Yeck, W. L. (2022). Beyond the Teleseism: Introducing Regional Seismic and Geodetic Data into Routine USGS Finite-Fault Modeling. *Seismological Research Letters*, *93*(6), 3308–3323. doi: 10.1785/0220220047

Golriz, D., Hirshorn, B., Bock, Y., Weinstein, S., & Weiss, J. R. (2023). Real-Time Seismogeodetic Earthquake Magnitude Estimates for Local Tsunami Warnings. *Journal of Geophysical Research: Solid Earth*, *128*(1), e2022JB025555. doi: 10.1029/2022JB025555

Gomez, C. (2024). The 1 January 2024 Noto Peninsula co-seismic landslides hazards: Preliminary results. *AUC Geographica*, *60*(1), 1–8. doi: 10.14712/23361980.2024.11

González, F. I., LeVeque, R. J., Chamberlain, P., Hirai, B., Varkovitzky, J., & George, D. L. (2011). Validation of the GeoClaw model. In (pp. 1–84). GeoClaw Tsunami Modeling Group University of Washington.

Gosselin, J. M., Audet, P., Estève, C., McLellan, M., Mosher, S. G., & Schaeffer, A. J. (2020). Seismic evidence for megathrust fault-valve behavior during episodic tremor and slip. *Science Advances*, *6*(4), eaay5174. doi: 10.1126/sciadv.aay5174

Gusman, A. R., & Tanioka, Y. (2014). W Phase Inversion and Tsunami Inundation Modeling for Tsunami Early Warning: Case Study for the 2011 Tohoku Event. *Pure and Applied Geophysics*, *171*(7), 1409–1422. doi: 10.1007/s00024-013-0680-z

Hamling, I. J., Hreinsdóttir, S., Clark, K., Elliott, J., Liang, C., Fielding, E., ... Stirling, M. (2017). Complex multifault rupture during the 2016 Mw 7.8 Kaikōura earthquake, New Zealand. *Science*, *356*(6334), eaam7194. doi: 10.1126/science.aam7194

Hastings, W. K. (1970). Monte Carlo sampling methods using Markov chains and their applications. *Biometrika*, *57*(1), 97–109. doi: 10.1093/biomet/57.1.97

Hirshorn, B., Weinstein, S., Wang, D., Koyanagi, K., Becker, N., & McCreery, C. (2020). Earthquake Source Parameters, Rapid Estimates for Tsunami Forecasts and Warnings. In R. A. Meyers (Ed.), *Encyclopedia of Complexity and Systems Science* (pp. 1–35). Berlin, Heidelberg: Springer. doi: 10.1007/978-3-642-27737-5_160-2

Hubbard, J. A., & Bradley, K. (2024). Seismicity patterns around the Jan 1 earthquake in Japan. *Earthquake Insights*. doi: 10.62481/72ea1b55

Hunter, J. D. (2007). Matplotlib: A 2D Graphics Environment. *Computing in Science & Engineering*, *9*(3), 90–95. doi: 10.1109/MCSE.2007.55

Ishiyama, T., Sato, H., Kato, N., Koshiya, S., Abe, S., Shiraishi, K., & Matsubara, M. (2017). Structures and active tectonics of compressionally reactivated back-arc failed rift across the Toyama trough in the Sea of Japan, revealed by multiscale seismic profiling. *Tectonophysics*, *710-711*, 21–36. doi: 10.1016/j.tecto.2016.09.029

Japan Meteorological Agency. (2024). *The Seismological Bulletin of Japan.* Retrieved from `https://www.data.jma.go.jp/svd/eqev/data/bulletin/hypo_e.html`

Ji, C., Wald, D. J., & Helmberger, D. V. (2002). Source Description of the 1999 Hector Mine, California, Earthquake, Part I: Wavelet Domain Inversion Theory and Resolution Analysis. *Bulletin of the Seismological Society of America*, *92*(4), 1192–1207. doi: 10.1785/0120000916

Jia, Z., Jin, Z., Marchandon, M., Ulrich, T., Gabriel, A.-A., Fan, W., ... Fialko, Y. (2023). The complex dynamics of the 2023 Kahramanmaraş, Turkey, Mw 7.8-7.7 earthquake doublet. *Science*, *381*(6661), 985–990. doi: 10.1126/science.adi0685

Jia, Z., Zhan, Z., & Kanamori, H. (2022). The 2021 South Sandwich Island Mw 8.2 Earthquake: A Slow Event Sandwiched Between Regular Ruptures. *Geophysical Research Letters*, *49*(3), e2021GL097104. doi: 10.1029/2021GL097104

Kanamori, H. (1993). W phase. *Geophysical Research Letters*, *20*(16), 1691–1694. doi: 10.1029/93GL01883

Kanamori, H., & Rivera, L. (2008). Source inversion of W phase: speeding up seismic tsunami warning. *Geophysical Journal International*, *175*(1), 222–238. doi: 10.1111/j.1365-246X.2008.03887.x

Kataoka, K., Urabe, A., Nishii, R., Matsumoto, T., Niiya, H., Watanabe, N., ... Miyabuchi, Y. (2024). Extensive liquefaction and building damage on the Niigata Plain due to the 1 January 2024 Noto Peninsula Earthquake: Geomorphological and geological aspects and land-use in coastal and lowland areas. Vienna, Austria: Copernicus Meetings. doi: 10.5194/egusphere-egu24-22541

Kato, A. (2024). Implications of Fault-Valve Behavior From Immediate Aftershocks Following the 2023 Mj6.5 Earthquake Beneath the Noto Peninsula, Central Japan. *Geophysical Research Letters*, *51*(1), e2023GL106444. doi:

10.1029/2023GL106444

Kato, A., & Nishimura, T. (2024). Foreshock sequence prior to the 2024 M7.6 Noto-Hanto earthquake, Japan. Vienna, Austria: Copernicus Meetings. doi: 10.5194/egusphere-egu24-22522

Kennett, B. L., & Engdahl, E. R. (1991). Traveltimes for global earthquake location and phase identification. *Geophysical Journal International*, *105*(2), 429–465. doi: 10.1111/J.1365-246X.1991.TB06724.X

Kikuchi, M., & Kanamori, H. (1982). Inversion of complex body waves. *Bulletin of the Seismological Society of America*, *72*(2), 491–506. doi: 10.1785/BSSA0720020491

Koshimura, S., Adriano, B., Mizutani, A., Mas, E., Ohta, Y., Nagata, S., ... Suzuki, T. (2024). The Impact of the 2024 Noto Peninsula Earthquake Tsunami. Vienna, Austria: Copernicus Meetings. doi: 10.5194/egusphere-egu24-22523

Krischer, L., Megies, T., Barsch, R., Beyreuther, M., Lecocq, T., Caudron, C., & Wassermann, J. (2015). ObsPy: a bridge for seismology into the scientific Python ecosystem. *Computational Science & Discovery*, *8*(1), 014003. doi: 10.1088/1749-4699/8/1/014003

Kutschera, F., Jia, Z., Oryan, B., Wong, J. W. C., Fan, W., & Gabriel, A.-A. (2024). *Supplementary material for "The Multi-Segment Complexity of the 2024 Mw 7.5 Noto Peninsula Earthquake Governing its Tsunami Generation"* [dataset]. Zenodo. doi: 10.5281/zenodo.13358788

Lee, S.-J., Huang, B.-S., Ando, M., Chiu, H.-C., & Wang, J.-H. (2011). Evidence of large scale repeating slip during the 2011 Tohoku-Oki earthquake. *Geophysical Research Letters*, *38*(19). doi: 10.1029/2011GL049580

Lee, S.-J., Ma, K.-F., & Chen, H.-W. (2006). Three-dimensional dense strong motion waveform inversion for the rupture process of the 1999 Chi-Chi, Taiwan, earthquake. *Journal of Geophysical Research: Solid Earth*, *111*(B11). doi: 10.1029/2005JB004097

Leonard, M. (2010). Earthquake Fault Scaling: Self-Consistent Relating of Rupture Length, Width, Average Displacement, and Moment Release. *Bulletin of the Seismological Society of America*, *100*(5A), 1971–1988. doi: 10.1785/0120090189

LeVeque, R. J., & George, D. L. (2008). High-Resolution Finite Volume Methods for the Shallow Water Equations With Bathymetry and Dry States. *Advanced Numerical Models for Simulating Tsunami Waves and Runup*, 43–73. doi: 10.1142/9789812790910_0002

LeVeque, R. J., George, D. L., & Berger, M. J. (2011). Tsunami modelling with adaptively refined finite volume methods. *Acta Numerica*, *20*, 211–289. doi: 10.1017/S0962492911000043

Liu, C. M., Rim, D., Baraldi, R., & LeVeque, R. J. (2021). Comparison of Machine Learning Approaches for Tsunami Forecasting from Sparse Observations. *Pure and Applied Geophysics*, *178*(12), 5129–5153. doi: 10.1007/s00024-021-02841-9

Lohman, R. B., & McGuire, J. J. (2007). Earthquake swarms driven by aseismic creep in the Salton Trough, California. *Journal of Geophysical Research: Solid Earth*, *112*(B4). doi: 10.1029/2006JB004596

Lotto, G. C., Jeppson, T. N., & Dunham, E. M. (2018). Fully Coupled Simulations of Megathrust Earthquakes and Tsunamis in the Japan Trench, Nankai Trough, and Cascadia Subduction Zone. *Pure and Applied Geophysics*, *176*(9), 4009–4041. doi: 10.1007/S00024-018-1990-Y

Ma, Z., Zeng, H., Luo, H., Liu, Z., Jiang, Y., Aoki, Y., ... Wei, S. (2024). Slow rupture in a fluid-rich fault zone initiated the 2024 Mw 7.5 Noto earthquake. *Science*, *0*(0). doi: 10.1126/science.ado5143

Madden, E. H., Ulrich, T., & Gabriel, A.-A. (2022). The State of Pore Fluid Pressure and 3-D Megathrust Earthquake Dynamics. *Journal of Geophysical Re-*

search: Solid Earth, *127*(4), e2021JB023382. doi: 10.1029/2021JB023382
Mandli, K. T., Ahmadia, A. J., Berger, M., Calhoun, D., George, D. L., Hadjimichael, Y., ... LeVeque, R. J. (2016). Clawpack: building an open source ecosystem for solving hyperbolic PDEs. *PeerJ Computer Science*, *2*(8), e68. doi: 10.7717/peerj-cs.68
Masuda, H., Sugawara, D., Cheng, A.-C., Suppasri, A., Shigihara, Y., Kure, S., & Imamura, F. (2024). Modeling the 2024 Noto Peninsula earthquake tsunami: implications for tsunami sources in the eastern margin of the Japan Sea. *Geoscience Letters*, *11*(1), 29. doi: 10.1186/s40562-024-00344-8
Matsushi, Y. (2024). Geomorphological consequences of the 2024 Noto Peninsula Earthquake: tectonic deformations, coseismic landslides, and their implications. Vienna, Austria: Copernicus Meetings. doi: 10.5194/egusphere-egu24-22535
Melgar, D., Allen, R. M., Riquelme, S., Geng, J., Bravo, F., Baez, J. C., ... Smalley Jr., R. (2016). Local tsunami warnings: Perspectives from recent large events. *Geophysical Research Letters*, *43*(3), 1109–1117. doi: 10.1002/2015GL067100
Melgar, D., & Ruiz-Angulo, A. (2018). Long-Lived Tsunami Edge Waves and Shelf Resonance From the M8.2 Tehuantepec Earthquake. *Geophysical Research Letters*, *45*(22), 12,414–12,421. doi: 10.1029/2018GL080823
Minson, S. E., & Dreger, D. S. (2008). Stable inversions for complete moment tensors. *Geophysical Journal International*, *174*(2), 585–592. doi: 10.1111/j.1365-246X.2008.03797.x
Miyoshi, T., Saito, T., Inazu, D., & Tanaka, S. (2015). Tsunami modeling from the seismic CMT solution considering the dispersive effect: a case of the 2013 Santa Cruz Islands tsunami. *Earth, Planets and Space*, *67*(1), 4. doi: 10.1186/s40623-014-0179-6
Mizutani, A., Adriano, B., Mas, E., & Koshimura, S. (2024). *Fault Model of the 2024 Noto Peninsula Earthquake Based on Aftershock, Tsunami, and GNSS Data.* Retrieved from https://www.researchsquare.com/article/rs-4167995/v1 doi: 10.21203/rs.3.rs-4167995/v1
MLIT. (2014). *Ministry of Land, Infrastructure, Transport and Tourism (MLIT): Research Committee on Large-Scale Earthquakes in the Sea of Japan (in Japanese, translated title).* Retrieved from https://www.mlit.go.jp/river/shinngikai_blog/daikibojishinchousa
Mori, N., Satake, K., Cox, D., Goda, K., Catalan, P. A., Ho, T.-C., ... Wilson, R. (2022). Giant tsunami monitoring, early warning and hazard assessment. *Nature Reviews Earth & Environment*, *3*(9), 557–572. doi: 10.1038/s43017-022-00327-3
Mulia, I. E., Heidarzadeh, M., Gusman, A. R., Satake, K., Fujii, Y., Sujatmiko, K. A., ... Windupranata, W. (2024). Compounding impacts of the earthquake and submarine landslide on the toyama bay tsunami during the january 2024 noto peninsula event. *Ocean Engineering*, *310*, 118698. doi: https://doi.org/10.1016/j.oceaneng.2024.118698
Murotani, S., Satake, K., & Fujii, Y. (2013). Scaling relations of seismic moment, rupture area, average slip, and asperity size for M 9 subduction-zone earthquakes. *Geophysical Research Letters*, *40*(19), 5070–5074. doi: 10.1002/grl.50976
Nielsen, S., & Madariaga, R. (2003). On the Self-Healing Fracture Mode. *Bulletin of the Seismological Society of America*, *93*(6), 2375–2388. doi: 10.1785/0120020090
Nielsen, S., Taddeucci, J., & Vinciguerra, S. (2010). Experimental observation of stick-slip instability fronts. *Geophysical Journal International*, *180*(2), 697–702. doi: 10.1111/j.1365-246X.2009.04444.x
Nishimura, T., Hiramatsu, Y., & Ohta, Y. (2023). Episodic transient deformation re-

vealed by the analysis of multiple GNSS networks in the Noto Peninsula, central Japan. *Scientific Reports*, *13*(1), 8381. doi: 10.1038/s41598-023-35459-z

Oike, K., & Huzita, K. (1988). Relation between characteristics of seismic activity and neotectonics in Honshu, Japan. *Tectonophysics*, *148*(1), 115–130. doi: 10.1016/0040-1951(88)90165-5

Okada, Y. (1985). Surface deformation due to shear and tensile faults in a half-space. *Bulletin of the Seismological Society of America*, *75*(4), 1135–1154. doi: 10.1785/BSSA0750041135

Okada, Y. (1992). Internal deformation due to shear and tensile faults in a half-space. *Bulletin of the Seismological Society of America*, *82*(2), 1018–1040. doi: 10.1785/BSSA0820021018

Okada, Y., Kasahara, K., Hori, S., Obara, K., Sekiguchi, S., Fujiwara, H., & Yamamoto, A. (2004). Recent progress of seismic observation networks in Japan —Hi-net, F-net, K-NET and KiK-net—. *Earth, Planets and Space*, *56*(8), xv–xxviii. doi: 10.1186/BF03353076

Okamura, Y., Ogami, T., Inoue, T., Sato, T., & Arimoto, J. (2024). *Tenth Report: Urgent Investigation Report on the 2024 Noto Peninsula Earthquake (Displacement of submarine active faults associated with the 2024 Noto Peninsula Earthquake).* Retrieved from `https://www.gsj.jp/hazards/earthquake/noto2024/noto2024-10.html`

Okuwaki, R., Yagi, Y., Murakami, A., & Fukahata, Y. (2024). A Multiplex Rupture Sequence Under Complex Fault Network Due To Preceding Earthquake Swarms During the 2024 Mw 7.5 Noto Peninsula, Japan, Earthquake. *Geophysical Research Letters*, *51*(11), e2024GL109224. doi: 10.1029/2024GL109224

Olalotiti-Lawal, F., & Datta-Gupta, A. (2018). A multiobjective Markov chain Monte Carlo approach for history matching and uncertainty quantification. *Journal of Petroleum Science and Engineering*, *166*, 759–777. doi: 10.1016/j.petrol.2018.03.062

O'Toole, T. B., Valentine, A. P., & Woodhouse, J. H. (2012). Centroid–moment tensor inversions using high-rate GPS waveforms. *Geophysical Journal International*, *191*(1), 257–270. doi: 10.1111/j.1365-246X.2012.05608.x

Qian, Y., Ni, S., Wei, S., Almeida, R., & Zhang, H. (2017). The effects of core-reflected waves on finite fault inversions with teleseismic body wave data. *Geophysical Journal International*, *211*(2), 936–951. doi: 10.1093/gji/ggx338

Qin, X., LeVeque, R. J., & Motley, M. R. (2019). Accelerating an Adaptive Mesh Refinement Code for Depth-Averaged Flows Using GPUs. *Journal of Advances in Modeling Earth Systems*, *11*(8), 2606–2628. doi: 10.1029/2019MS001635

Ray, A., Alumbaugh, D. L., Hoversten, G. M., & Key, K. (2013). Robust and accelerated Bayesian inversion of marine controlled-source electromagnetic data using parallel tempering. *Geophysics*, *78*(6), E271–E280. doi: 10.1190/geo2013-0128.1

Rice, J. R. (1992). Chapter 20 Fault Stress States, Pore Pressure Distributions, and the Weakness of the San Andreas Fault. In B. Evans & T.-f. Wong (Eds.), *International Geophysics* (Vol. 51, pp. 475–503). Academic Press. doi: 10.1016/S0074-6142(08)62835-1

Rim, D., Baraldi, R., Liu, C. M., LeVeque, R. J., & Terada, K. (2022). Tsunami Early Warning From Global Navigation Satellite System Data Using Convolutional Neural Networks. *Geophysical Research Letters*, *49*(20), e2022GL099511. doi: 10.1029/2022GL099511

Romano, F., Gusman, A. R., Power, W., Piatanesi, A., Volpe, M., Scala, A., & Lorito, S. (2021). Tsunami Source of the 2021 MW 8.1 Raoul Island Earthquake From DART and Tide-Gauge Data Inversion. *Geophysical Research Letters*, *48*(17), e2021GL094449. doi: 10.1029/2021GL094449

Ross, Z. E., Cochran, E. S., Trugman, D. T., & Smith, J. D. (2020). 3D fault architecture controls the dynamism of earthquake swarms. *Science*, *368*(6497), 1357–1361. doi: 10.1126/science.abb0779

Sambridge, M., & Mosegaard, K. (2002). Monte Carlo Methods in Geophysical Inverse Problems. *Reviews of Geophysics*, *40*(3), 3–1–3–29. doi: 10.1029/2000RG000089

Satake, K., Ishibe, T., Murotani, S., Mulia, I. E., & Gusman, A. R. (2022). Effects of uncertainty in fault parameters on deterministic tsunami hazard assessment: examples for active faults along the eastern margin of the Sea of Japan. *Earth, Planets and Space*, *74*(1), 36. doi: 10.1186/s40623-022-01594-6

Sato, H., Ishiyama, T., Hashima, A., Kato, N., Van-Horne, A., Claringbould, J. S., … Koshiya, S. (2020). Development of active fault model. *Annual Progress Reports of the Integrated Research Project on Seismic and Tsunami Hazards around the Sea of Japan (FY2019)*, 209–239.

Seabold, S., & Perktold, J. (2010). Statsmodels: Econometric and Statistical Modeling with Python. In (pp. 92–96). Austin, Texas. doi: 10.25080/Majora-92bf1922-011

Selva, J., Lorito, S., Volpe, M., Romano, F., Tonini, R., Perfetti, P., … Amato, A. (2021). Probabilistic tsunami forecasting for early warning. *Nature Communications*, *12*(1), 1–14. doi: 10.1038/s41467-021-25815-w

Sepúlveda, I., Tozer, B., Haase, J. S., Liu, P. L.-F., & Grigoriu, M. (2020). Modeling Uncertainties of Bathymetry Predicted With Satellite Altimetry Data and Application to Tsunami Hazard Assessments. *Journal of Geophysical Research: Solid Earth*, *125*(9), e2020JB019735. doi: 10.1029/2020JB019735

Shelly, D. R. (2024). Examining the Connections Between Earthquake Swarms, Crustal Fluids, and Large Earthquakes in the Context of the 2020–2024 Noto Peninsula, Japan, Earthquake Sequence. *Geophysical Research Letters*, *51*(4), e2023GL107897. doi: 10.1029/2023GL107897

Sibson, R. H. (1992). Implications of fault-valve behaviour for rupture nucleation and recurrence. *Tectonophysics*, *211*(1), 283–293. doi: 10.1016/0040-1951(92)90065-E

Suppasri, A., Kitamura, M., Alexander, D., Seto, S., & Imamura, F. (2024). The 2024 Noto Peninsula earthquake: Preliminary observations and lessons to be learned. *International Journal of Disaster Risk Reduction*, *110*, 104611. doi: 10.1016/j.ijdrr.2024.104611

Tanaka, Y., Ohta, Y., & Miyazaki, S. (2019). Real-Time Coseismic Slip Estimation via the GNSS Carrier Phase to Fault Slip Approach: A Case Study of the 2016 Kumamoto Earthquake. *Geophysical Research Letters*, *46*(3), 1367–1374. doi: 10.1029/2018GL080741

Tarantola, A. (2005). *Inverse Problem Theory and Methods for Model Parameter Estimation.* Society for Industrial and Applied Mathematics. doi: 10.1137/1.9780898717921

Taufiqurrahman, T., Gabriel, A.-A., Li, D., Ulrich, T., Li, B., Carena, S., … Gallovič, F. (2023). Dynamics, interactions and delays of the 2019 Ridgecrest rupture sequence. *Nature*, *618*, 308–315. doi: 10.1038/s41586-023-05985-x

The Headquarters for Earthquake Research Promotion. (2024). *Evaluation of the 2024 Noto Peninsula Earthquake (in Japanese).* Retrieved from `https://www.jishin.go.jp/evaluation/seismicity_monthly`

Thompson, E. M., McBride, S. K., Hayes, G. P., Allstadt, K. E., Wald, L. A., Wald, D. J., … Grant, A. R. R. (2019). USGS Near-Real-Time Products—and Their Use—for the 2018 Anchorage Earthquake. *Seismological Research Letters*, *91*(1), 94–113. doi: 10.1785/0220190207

Tong, X., Sandwell, D. T., & Fialko, Y. (2010). Coseismic slip model of the 2008 Wenchuan earthquake derived from joint inversion of interferometric synthetic aperture radar, GPS, and field data. *Journal of Geophysical Research: Solid Earth*, *115*(B4). doi: 10.1029/2009JB006625

Tsai, V. C., Nettles, M., Ekström, G., & Dziewonski, A. M. (2005). Multiple CMT source analysis of the 2004 Sumatra earthquake. *Geophysical Research Letters*, *32*(17). doi: 10.1029/2005GL023813

Ueno, H. (2002). Improvement of hypocenter determination procedures in the Japan Meteorological Agency. *QJ Seismol.*, *65*, 123–134.

Ulrich, T., Gabriel, A. A., & Madden, E. H. (2022). Stress, rigidity and sediment strength control megathrust earthquake and tsunami dynamics. *Nature Geoscience*, *15*(1), 67–73. doi: 10.1038/s41561-021-00863-5

U.S. Geological Survey. (2024). *M 7.5 - 2024 Noto Peninsula, Japan Earthquake.* Retrieved from `https://earthquake.usgs.gov/earthquakes/eventpage/us6000m0xl/executive`

Wald, D. J., Helmberger, D. V., & Hartzell, S. H. (1990). Rupture process of the 1987 Superstition Hills earthquake from the inversion of strong-motion data. *Bulletin of the Seismological Society of America*, *80*(5), 1079–1098. doi: 10.1785/BSSA0800051079

Wang, D., Becker, N. C., Walsh, D., Fryer, G. J., Weinstein, S. A., McCreery, C. S., … Shiro, B. (2012). Real-time forecasting of the April 11, 2012 Sumatra tsunami. *Geophysical Research Letters*, *39*(19). doi: 10.1029/2012GL053081

Wang, Y., Heidarzadeh, M., Satake, K., Mulia, I. E., & Yamada, M. (2020). A Tsunami Warning System Based on Offshore Bottom Pressure Gauges and Data Assimilation for Crete Island in the Eastern Mediterranean Basin. *Journal of Geophysical Research: Solid Earth*, *125*(10), e2020JB020293. doi: 10.1029/2020JB020293

Wessel, P. (2024). The Origins of the Generic Mapping Tools: From Table Tennis to Geoscience. *Perspectives of Earth and Space Scientists*, *5*(1), e2023CN000231. doi: 10.1029/2023CN000231

Wirp, A. S., Gabriel, A. A., Schmeller, M., H. Madden, E., van Zelst, I., Krenz, L., … Rannabauer, L. (2021). 3D Linked Subduction, Dynamic Rupture, Tsunami, and Inundation Modeling: Dynamic Effects of Supershear and Tsunami Earthquakes, Hypocenter Location, and Shallow Fault Slip. *Frontiers in Earth Science*, *9*, 177. doi: 10.3389/feart.2021.626844

Xu, L., Ji, C., Meng, L., Ampuero, J.-P., Yunjun, Z., Mohanna, S., & Aoki, Y. (2024). Dual-initiation ruptures in the 2024 Noto earthquake encircling a fault asperity at a swarm edge. *Science*, *385*(6711), 871–876. doi: 10.1126/science.adp0493

Xu, L., Mohanna, S., Meng, L., Ji, C., Ampuero, J.-P., Yunjun, Z., … Liang, C. (2023). The overall-subshear and multi-segment rupture of the 2023 Mw7.8 Kahramanmaraş, Turkey earthquake in millennia supercycle. *Communications Earth & Environment*, *4*(1), 1–13. doi: 10.1038/s43247-023-01030-x

Yagi, Y., & Fukahata, Y. (2011). Rupture process of the 2011 Tohoku-oki earthquake and absolute elastic strain release. *Geophysical Research Letters*, *38*(19). doi: 10.1029/2011GL048701

Yang, S., Sang, C., Hu, Y., & Wang, K. (2024). Coseismic and Early Postseismic Deformation of the 2024 Mw7.45 Noto Peninsula Earthquake. *Geophysical Research Letters*, *51*(11), e2024GL108843. doi: 10.1029/2024GL108843

Yao, H., Gerstoft, P., Shearer, P. M., & Mecklenbräuker, C. (2011). Compressive sensing of the Tohoku-Oki Mw 9.0 earthquake: Frequency-dependent rupture modes. *Geophysical Research Letters*, *38*(20). doi: 10.1029/2011GL049223

Yoshida, K., Uchida, N., Matsumoto, Y., Orimo, M., Okada, T., Hirahara, S., … Hino, R. (2023). Updip Fluid Flow in the Crust of the Northeastern Noto Peninsula, Japan, Triggered the 2023 Mw 6.2 Suzu Earthquake During Swarm Activity. *Geophysical Research Letters*, *50*(21), e2023GL106023. doi: 10.1029/2023GL106023

Zal, H. J., Jacobs, K., Savage, M. K., Yarce, J., Mroczek, S., Graham, K., … Henrys, S. (2020). Temporal and spatial variations in seismic anisotropy and

$V\mathrm{P}/V\mathrm{S}$ ratios in a region of slow slip. *Earth and Planetary Science Letters*, *532*, 115970. doi: 10.1016/j.epsl.2019.115970

Zheng, X., Zhang, Y., Wang, R., Zhao, L., Li, W., & Huang, Q. (2020). Automatic Inversions of Strong-Motion Records for Finite-Fault Models of Significant Earthquakes in and Around Japan. *Journal of Geophysical Research: Solid Earth*, *125*(9), e2020JB019992. doi: 10.1029/2020JB019992

Zhu, L., & Rivera, L. A. (2002). A note on the dynamic and static displacements from a point source in multilayered media. *Geophysical Journal International*, *148*(3), 619–627. doi: 10.1046/j.1365-246X.2002.01610.x

Zhu, W., Allison, K. L., Dunham, E. M., & Yang, Y. (2020). Fault valving and pore pressure evolution in simulations of earthquake sequences and aseismic slip. *Nature Communications*, *11*(1), 4833. doi: 10.1038/s41467-020-18598-z